

# Enhanced Exosome Immunodetection by Integration of Silica Inverse Opal Architectures as Nanostructured Sensors in Quartz Crystal Microbalance with Dissipation Monitoring.

Jugal Suthar,<sup>a,b</sup> Alberto Alvarez-Fernandez,<sup>a,\*</sup> Alaric Taylor,<sup>a</sup> Gareth R. Williams,<sup>b</sup> and Stefan Guldin.<sup>a,\*</sup>

Exosomes are nanosized circulating vesicles that contain biomarkers considered promising for early diagnosis within neurology, cardiology and oncology. Recently, acoustic wave biosensors, in particular based on quartz crystal microbalance with dissipation monitoring (QCM-D), have emerged as a sensitive, label-free, and selective exosome characterisation platform. A rational approach to further improving sensing detection limits relies on the nanostructuring of the sensor surfaces. To this end, inorganic inverse opals (IOs) derived from colloidal self-assembly present a highly tuneable and scalable nanoarchitecture of suitable feature sizes and surface chemistry. This work systematically investigates their use in 2D and 3D for enhanced QCM-D exosome detection. Precise tuning of the architecture parameters delivered improvements in detection performance to sensitivities as low as  $6.24 \times 10^7$  particles/ml. Our findings emphasise that attempts to enhance acoustic immunosensing via increasing the surface area by 3D nanostructuring need to be carefully analyzed in order to exclude solvent and artefact entrapment effects. Moreover, the use of 2D nanostructured electrodes to compartmentalise analyte anchoring presents a particularly promising design principle.

## Introduction

Exosomes are an endogenously produced subset of extracellular vesicles that are released from cells as part of their routine processing.<sup>1,2</sup> Depending on the cell of origin, exosomes are found to carry biomolecular content that is essential for intercellular communication and disease propagation, in the form of proteins, DNA, RNA, and lipids.<sup>3,4</sup> Evidence now demonstrates that the detection and quantification of exosomes can help in the elucidation of pathological pathways of many diseases, particularly within neurology, cardiology, and oncology, emphasizing the necessity to establish sensitive, specific and reproducible exosome detection techniques.<sup>5–7</sup> X-ray scattering,<sup>8</sup> fluorescence spectroscopy,<sup>9</sup> Raman spectroscopy,<sup>10</sup> or electrochemical measurements<sup>11</sup> are just some of the novel exosome characterisation approaches recently reported. However, in general, none of these techniques currently meets the combination of prerequisites on detection limit, specificity, label-free recognition and minimal sample volume. As a result, current approaches lack the sensitivity of detecting at clinically relevant biomarker concentrations; are unable to discern reliably between exosome and non-exosome artefacts with increasing risk of

false-positive results; require diagnostic reagents for labelling that increase the assay complexity and cost; and/or are unsuitable for minimally invasive liquid biopsies because of the requisite sample volume.

A particularly promising analytical principle for multimodal biosensing is based on acoustic resonance.<sup>12</sup> The application of a quartz crystal microbalance with dissipation monitoring (QCM-D) has been shown to uniquely leverage differences between exosomes and associated contaminants in colloidal suspension by assessing both mass and viscoelastic properties, thus offering a superior level of analytical discrimination. The dual-mechanisms of measurement offered by QCM-D helped to overcome the current limitations of specificity within the exosome sensing field, providing an important addition to the characterisation toolkit. Specifically, the immunocapture of CD63-positive exosomes on gold-coated QCM sensor surfaces induced a dampening of shear wave oscillation of the QCM sensor due to the mass of the analyte. This was witnessed alongside a concomitant increase in dissipation, attributed to the soft, viscoelastic, nature of the exosomes. These are bound as discrete particles that also undergo rocking and translational movement, incurring energy loss at the sensor surface.<sup>13</sup> These findings have built upon previous citations demonstrating surface acoustic wave detection of exosomes that only offer a single mode of measurement.<sup>14</sup>

Despite the fact that QCM-D offers rich data on the build-up of functional interfaces, its limit-of-detection (LOD) remains relatively high ( $1.4 \times 10^8$  particles/mL). Therefore, whilst the technique presents a valuable complementary tool for biosensor development, further improvements are required in terms of detection sensitivity to effectively integrate QCM-D

<sup>a</sup> Department of Chemical Engineering, University College London, Torrington Place, London, WC1E 7JE, United Kingdom. E-mail: alberto.fernandez@ucl.ac.uk; s.guldin@ucl.ac.uk

<sup>b</sup> UCL School of Pharmacy, University College London, 29-39 Brunswick Square, Bloomsbury, London, WC1N 1AX, United Kingdom.

Supplementary Information (SI) available: including experimental setup, GISAXS, SEM image analysis, and further QCM-D data.

within minimally invasive disease diagnostics. This was partly achieved by coupling the QCM-D assessment with tandem electrochemical impedance measurements via an EQCM-D based detection platform (LOD  $6.7 \times 10^7$  particles/mL),<sup>15</sup> but further efforts are needed.

An alternative route to further improve analytical sensitivity and specificity in QCM-D is via nanostructuring of the electrode surface, with the rationale being to increase the sensing surface area (surface-to-volume ratio) for enhanced binding capacity and/or to modify the aspect ratio (length to diameter ratio) for optimal ligand arrangement.

In this context, inorganic inverse opals (IOs) derived by colloidal self-assembly present a highly tuneable and scalable nanoarchitecture of suitable feature sizes and surface chemistry.<sup>16–18</sup> IOs are three-dimensional porous structures with a regular arrangement of interconnected spheroid cavities that have a large internal surface area and a uniformity in pore size (ranging between 100–1000 nm) on the macroscale.<sup>19</sup> These properties make them ideal candidates for a myriad of applications, such as in catalytic systems,<sup>20,21</sup> photonics,<sup>22,23</sup> electrochemistry and energy devices.<sup>24–26</sup> 3D inverse opals (3D IOs) may be fabricated by top-down techniques such as photo- and electron beam lithography or nanoimprinting,<sup>27,28</sup> or via bottom-up techniques such as colloidal assembly with sacrificial spheres.<sup>29,30</sup> One particularly attractive route is by co-assembly, where an inorganic sol-gel precursor is added to a colloidal suspension and therefore participates in an evaporative self-assembly process at the meniscus of a substrate. The result is minimised cracking and inhomogeneities associated with the multistep process of standard colloidal assembly.<sup>31,32</sup> While colloids offer precise control over porous networks on the 100 nm to micrometres length scale, co-assembly techniques involving block copolymer micelles are particularly suited for pore diameters below 100 nm.<sup>33–37</sup>

The establishment of such precise and facile manufacturing methods for 3D IOs has facilitated their integration into biosensing.<sup>38</sup> The enhanced surface area offered by the incorporation of 3D IO structures, in combination with their optical properties, has been successfully exploited for improving the analytical performance of multiple sensing platforms. To this end, Li and co-workers developed a label-free biosensor based on  $\text{TiO}_2$  inverse opal films and reflectometry interference spectroscopy.<sup>39</sup> The physical adsorption of proteins on the pore surface was monitored by the shift in the reflection peak, allowing detection limits as low as  $1 \mu\text{g mL}^{-1}$ . Following a similar approach, Lee et al. successfully immobilised antibodies onto silica 3D IO nanostructures to create a label-free optical immunosensor capable of detecting influenza viruses with high sensitivity ( $10^3 - 10^5$  plaque-forming units) and specificity.<sup>40</sup> Other examples of IO-based biosensors include an immunosorbent assay built on an amylase-based enzymatic 3D IOs,<sup>41</sup> and a DNA sensor based on the immobilisation of fluorescent aptamers to 3D IO silica structures.<sup>42</sup> Of closer relevance to the work described herein, Dong et al. created gold-coated  $\text{TiO}_2$  3D IOs to successfully capture exosomes and obtain spectroscopic information from bonds within exosomal phosphoproteins, enabling specific differentiation between

exosomes isolated from cancer patients and healthy individuals.<sup>43</sup>

Despite these encouraging works, the application of 2D and 3D nanostructuring for QCM-D has not been extensively studied. Da Kyeong Oh and co-workers have shown improved specificity, faster kinetics, and higher sensitivity with the introduction of two- and three-dimensional molecularly imprinted polymers on 2D IOs for recognition of Bisphenol A and macromolecular proteins, respectively.<sup>44,45</sup> Other nanoarchitectures such as anodic aluminium oxide, or ZnO nanotips have been used to increase the surface area of the QCM-d sensor against different targets (such as enzymes,<sup>46</sup> liposomes,<sup>47</sup> and antibodies<sup>48</sup>) or for enhanced cell adhesion and proliferation.<sup>49</sup> However, the application of nanostructured surfaces for QCM-d based exosome biosensing remains unexplored. Moreover, solvent and artefact entrapment effects on the 2D and 3D nanostructured sensing surfaces have been constantly disregarded, preventing their full validation for real-world applications.

In response, this work explores the formation of IO porous structures atop QCM-D silica sensors for exosome detection. Through the optimisation of two different colloidal co-assembly methods (a vertical withdrawal and an evaporative deposition technique), FCC structured silica inverse opals without cracks and low defect density were successfully formed in 2D and 3D. Scanning electron microscopy (SEM) and grazing-incidence small-angle X-ray scattering (GISAXS) were used to confirm the structural properties of the created structures, including layer thickness, pore size and porosity. The impact of these parameters on detection sensitivity was subsequently investigated on a QCM-D platform, following silane-based functionalisation of the silica surfaces and immunocapture of CD63-positive exosomes in complex media. Evaluation of detection limits for mono- and multi-layer inverse opals and flat silica surfaces was achieved by determining their contributions to background (non-specific) signals.

## Results

### Size exclusion chromatography (SEC) isolation of exosomes from cell culture media

Prior to the detection of exosomes on silica substrates, effective isolation from cell culture media was achieved through the implementation of a SEC protocol. Nanoparticle tracking analysis (NTA) analysis of the 10 eluted SEC fractions identified fraction 4 as possessing the highest concentration of exosome sized particles (ESPs) per mL. Concentrations of ESPs reduced steadily in subsequent fractions (**Figure 1A**). This designated fraction 4 for further analysis and confirmed exosome presence. The size distribution profile of the particles in fraction 4 confirmed >91% of particles as being ESPs, with a modal size of 98 nm (**Figure 1B**). Western blot analysis successfully identified enriched exosomal proteins, namely CD81, Alix and CD63 (**Figure 1C**). This confirmed exosome presence amongst the ESPs but also that the vesicles possessed good biological integrity. Moreover, it ensured that CD63 was in sufficient abundance to be used as the target protein molecule for subsequent immuno-detection.

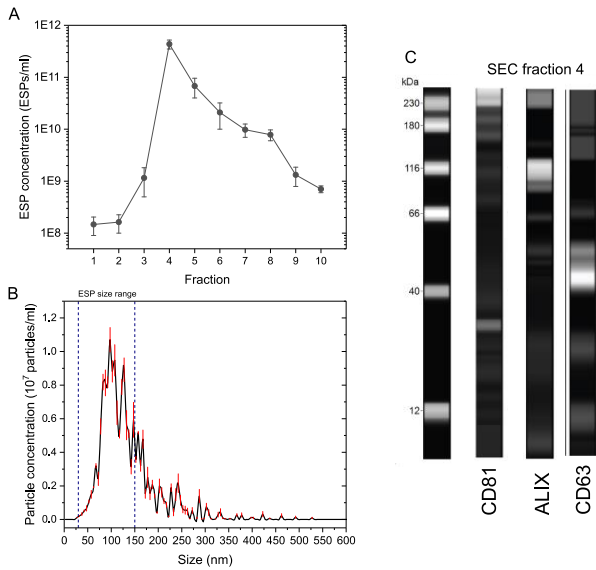


Figure 2: Concentration and particle size characterisation of ESP obtained via a SEC protocol. (A) ESP concentration of SEC fractions. Standard deviation determined from three independent experiments. (B) Particle size distribution of SEC fraction 4. (C) Capillary gel-based electrophoresis western blot of SEC fraction 4, identifying exosome enriched proteins, CD81 (26 kDa), Alix (93 kDa) and CD63 (57 kDa).

### Inverse opal structure formation

Inverse opal (IO) structures with different pore sizes and thicknesses were obtained following the methodology illustrated in **Figure 2**. As a first step, co-assembly of poly(methyl methacrylate) (PMMA) colloidal spheres (of two different diameters: 250 and 600 nm respectively) along with a silicate containing sol-gel solution was achieved using two approaches: vertical withdrawal (for 250 nm diameter spheres) and evaporative deposition (600 nm spheres). The sample holder apparatus for both techniques is displayed in **Figure S1**. Vertical withdrawal involved immersing a silica-coated substrate in the co-assembly mixture at room temperature. The

capillary forces at the meniscus that drive the assembly of the spheres and entrapment of the sol-gel matrix (hydrolysed tetraethyl orthosilicate) in-between. Evaporative deposition used elevated temperatures to initiate assembly. After the deposition was complete (substrate withdrawn or mixture evaporated), opal structures (crystals) were subject to O<sub>2</sub> ion etching (post-vertical withdrawal) or calcination (post-evaporative deposition) to remove the PMMA colloidal spheres and reveal the inorganic SiO<sub>2</sub> IO network of pores. The rationale for selecting larger PMMA spheres for multilayer IOs was to provide sufficient pore and neck size for larger ESPs to infiltrate deeper within the porous network.

### Inverse opal structure characterisation

Top-view SEM images of the IO structures obtained after polymer removal show in both cases a crack-free and homogeneous porous structure. IOs produced via the vertical withdrawal method present a monolayer configuration, with excellent ordering as confirmed by FFT analysis (**Figure 3A and C**). This type of surface could provide the analyte with direct access to the underlying substrate and ensure that bound analytes are kept at a close distance to the oscillatory surface. IOs structures fabricated following the evaporative deposition approach produced a multilayer IO structure with a thickness of approximately 1500 nm (**Figure 3B and D**). The geometrical architecture of the close-packed pore structure could increase the tortuosity for analytes to reach the sensor surface and provide a greater internal surface area for immune-functionalisation. The structural order of the 3D IO was further confirmed by small-angle x-ray scattering, displaying a face-centred cubic (FCC) structure with the {111} plane being parallel to the surface.<sup>50–52</sup> Furthermore, films were seen to grow along the {110} direction of the deposited FCC structure (**Figure S2**).

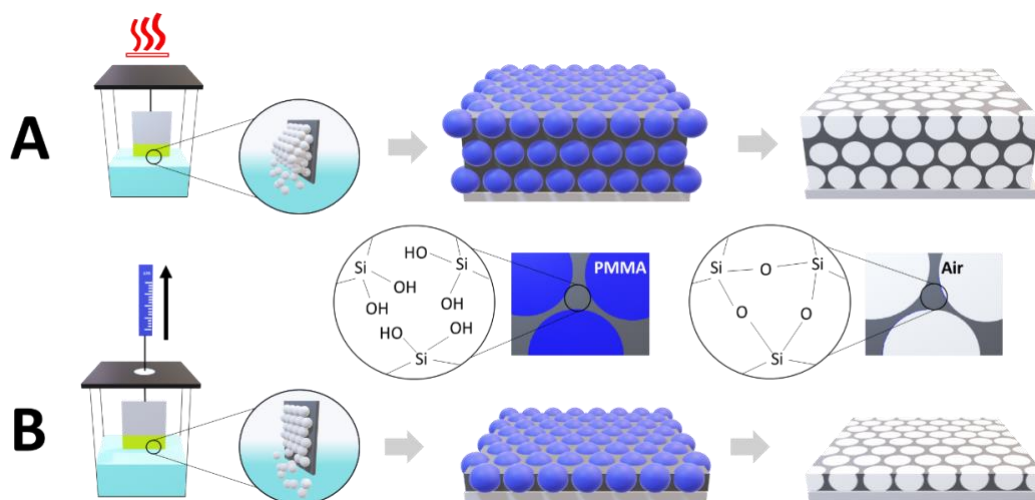


Figure 1: Schematic representation of implemented colloidal co-assembly methods and resulting inverse-opal structures. (A) Evaporative deposition for multi-layered IO formation approach. (B) Vertical withdrawal for monolayer formation.

slow withdrawal of the substrate at 0.01 mm/min created

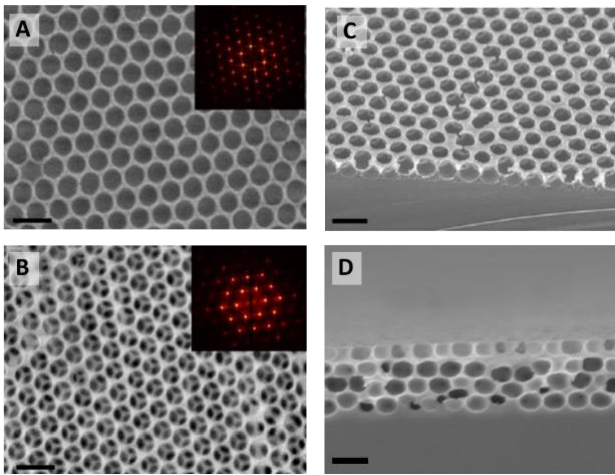


Figure 3: Top-view SEM micrographs of (A) inverse opal monolayer (scale bar: 400 nm) and (B) inverse opal multilayer (scale bars: 1 μm). Insets: FFT of respective SEM image. Cross-section SEM images of (C) monolayer and (D) multilayer IO architectures.

Image analysis of the top-view SEM images (via the software Pebbles)<sup>53</sup> enabled the calculation of average pore size distribution and total porosity in both structures. Monolayer IO pores were found to have a modal pore size of 247±3 nm, which suggests minimal shrinkage from the original 250 nm PMMA sphere size during the ion etching process (Figure S3A). Multilayer IO pores displayed an estimated surface diameter of 494±5 nm, which confirmed significant (17.7%) shrinkage of

pores compared to the original 600 nm PMMA sphere size, during the calcination process (Figure S3B). This is in line with previous studies and may be linked to the concurrent volume shrinkage of PMMA spheres and sol-gel precursors during the condensation reaction upon heating.<sup>54,55</sup>

Pore size analysis of the cross-sectional SEM image of the multilayer IO suggests that the shrinkage of the pores occurred with a directional bias, with the modal height being 381±4 nm, representing a 36.5% shrinkage (Figure S3C). The full pore width by comparison was determined to be 501±3 nm, marking a 16.5% shrinkage and highlighting significant pore anisotropy to give an oblate ellipsoid (Figure S3D). In terms of total porosity, values of 73.1% (IO monolayer) and 64.7% (3D IO) were calculated. Both results are in line with conventionally reported porosity values for FCC structured inverse opals.<sup>32</sup>

In a subsequent step, the internal surface area of both IO monolayer and multilayer was estimated using previous structural information. The internal surface area for a single oblate ellipsoidal pore within the multilayer structure can be calculated following Equation 1.

$$S = 4\pi \left( \frac{(ab)^{1.6} + (ac)^{1.6} + (bc)^{1.6}}{3} \right)^{-1.6} \quad (1)$$

Where  $S$  is the surface area,  $a$  and  $b$  represent the in-plane radial dimensions, and  $c$  being the out-of-plane dimension from ellipsoid centre to its surface.

Using structural values previously calculated by SEM, the total internal surface area for multilayer IO films was established at

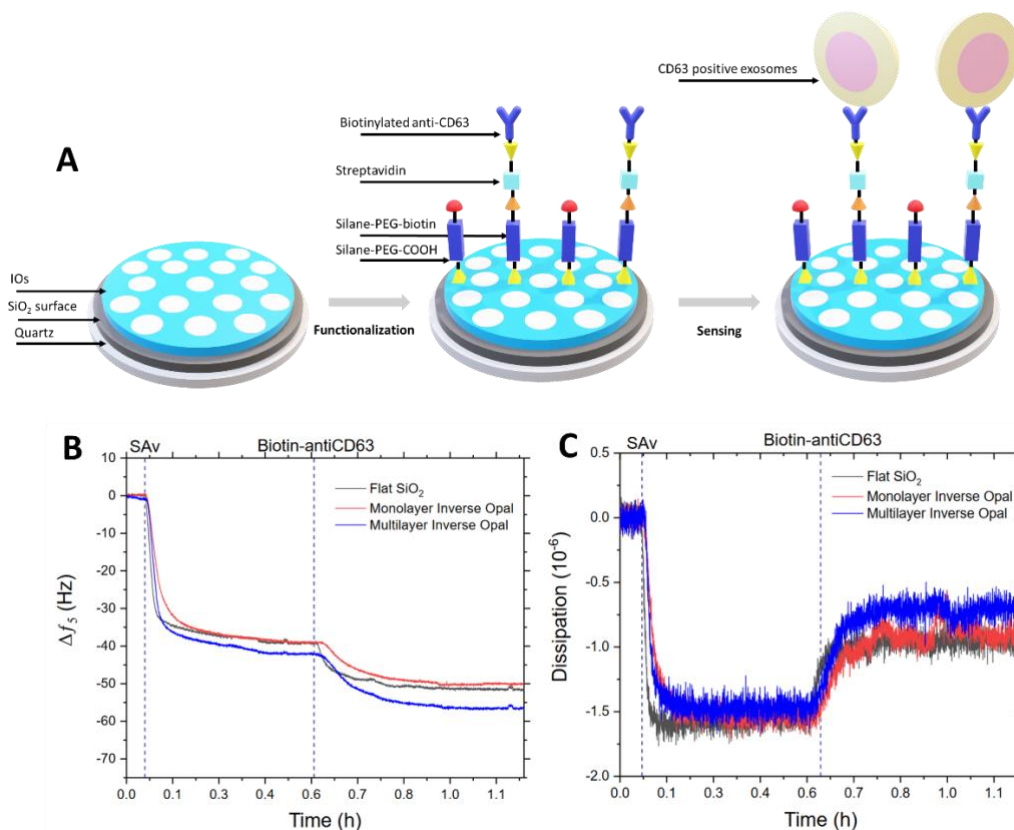


Figure 4: (A) Schematic representation of immunosensor fabrication atop IO coated sensors. QCM-D frequency (B) and dissipation (C) profiles captured for immunosensor fabrication process on flat silica substrates compare with IO monolayer and multilayer.

~215  $\mu\text{m}^2$ , marking a 43-fold increase in surface area compared a 5  $\mu\text{m}^2$  flat silica surface. A similar calculation for the monolayer IOs was also made, although a correction was applied by halving the figure to account the fact of the hemispherical shape of the obtained open porous monolayer. In comparison, the equivalent total internal surface area of the pores formed from the smaller 250 nm spheres was estimated to be ~9.9  $\mu\text{m}^2$ , i.e., a doubling of surface area. This underlines the scope for significant increases in detection surface area that IO structures offer.

### 3D IO modified sensors for QCM-D detection of exosomes

IO structures were applied to QCM sensors to understand the impact on the detection of ESP using the QCM-D platform and an immunosensing method, following the methodology displayed in **Figure 4A**. Silane-based chemistry was initially used to functionalised flat, monolayer IO and multilayer IO silica surfaces with a mixed-SAM that presents biotin molecules for subsequent streptavidin (Sav) fabrication. The QCM-D response to the fabrication process is shown in **Figure 4B-C**, confirming the adsorption of the relevant immuno-detection layers. No significant difference in response was seen between the surface architectures, however, the multilayer IO structure did exhibit marginally higher binding of the anti-CD63 antibody, which could be a result of its increased internal surface area. After functionalisation, the performance of all three surfaces was assessed against a spiked concentration of CD63 protein. **Figure 5A-B** shows that an incremental increase in response occurs with the increasing internal surface area of the structure. The monolayer exhibited a marginal improvement in CD63 detection compared to the flat silica, while the multilayer IO increased the response further by approximately 30% in terms of frequency change. Dissipation changes upon addition of

CD63 were small in nature, which was expected due to the largely non-viscoelastic properties of the spiked protein. This suggests that the protein was able to bind rigidly to the IO structure, irrespective of layer thickness. Spiked CD63 is a small molecule (2.4 nm) compared to the pore size, and thus would not induce any pore blockage but would be likely infiltrate the entire IO structure through inter-pore necks.

The detection of the considerably larger, fluid-filled, ESP structures on these surfaces was explored via the addition of  $5 \times 10^8$  ESPs/mL in 25% v/v serum (**Figure 5C-D**). The net decrease in frequency following a post-adsorption rinse signified the adsorption of particles to all three sensor surfaces, the most significant of which was seen with the multilayer IO structure, offering almost a 100% and 40% increase in response compared to flat and monolayer IO surfaces respectively (**Figure 5C**). The corresponding improvement in dissipation is also detected (**Figure 5D**).

To gain more insight into the ESP binding process across the different architectures, dissipation change was assessed as a function of frequency for ESP adsorption and rinse steps (**Figure 6**). All three sensor surfaces demonstrated an initial linear relationship between dissipation and frequency as ESPs are captured, with a subsequent decrease in relative dissipation response as the surface nears saturation. The follow-up rinsing of the sensor surface resulted in significant frequency and dissipation reduction for both flat and monolayer IO surfaces, indicating comprehensive removal of many loosely bound, or non-specifically adsorbed, artefacts from the sensing surface. These are assumed to be the serum content of the running buffer. In contrast, the multilayer IO sensor exhibited a stunted removal of such artefacts and a prolonged period of frequency reduction alongside a minimal decrease in dissipation. This may be a result of the continual removal of surface-bound contaminants, albeit to a lesser extent. Moreover, the thickness and interconnectivity of the multilayer IO could result in the entrapment of artefacts and small non-ESP particles within the porous network, which contributed to the elevated dissipation signal.

To substantiate this theory, control investigations were conducted by flowing  $1 \times 10^9$  ESPs/mL in HBS buffer and 25% v/v serum across the three surface types following functionalisation with a non-specific IgG control antibody, to determine the background non-specific binding contribution to the overall response. **Figure S4** indicates that the introduction of the sample to the sensor surface caused a small yet significant response in frequency and dissipation for multilayer IO surfaces (particularly in more complex media), whilst monolayer IOs demonstrate negligible change. It is possible that the multilayer architecture entrapped a greater volume of sample, increasing the oscillatory mass. Responses seen with multilayer IOs should therefore be approached with caution along with the knowledge of buffer composition.

Subsequently, the sensing performance of the IO architectures was explored across a range of ESP concentrations to determine

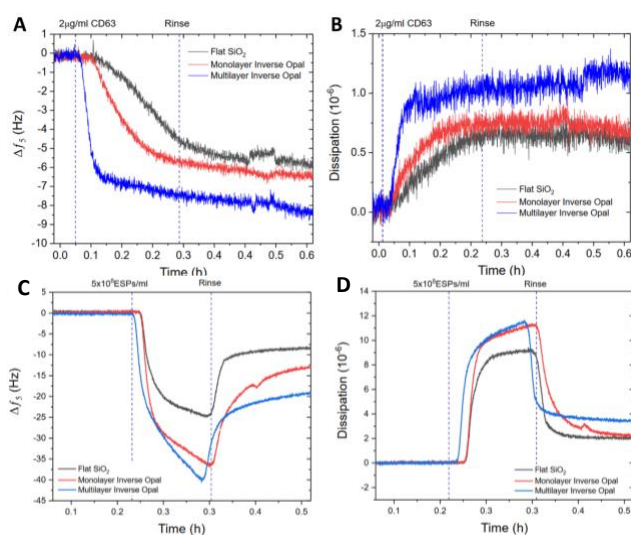


Figure 5: Comparison of frequency (A) and dissipation (B) profiles for 2  $\mu\text{g/ml}$  CD63 detection on flat silica, inverse opal monolayer and multilayer surfaces. QCM-D analysis of exosome detection using IO immunofunctionalised sensors. QCM-D frequency (C) and dissipation (D) profiles comparing responses to CD63-positive exosomes in 25% v/v human serum of flat silica, silica inverse opal monolayer and multilayer surfaces.

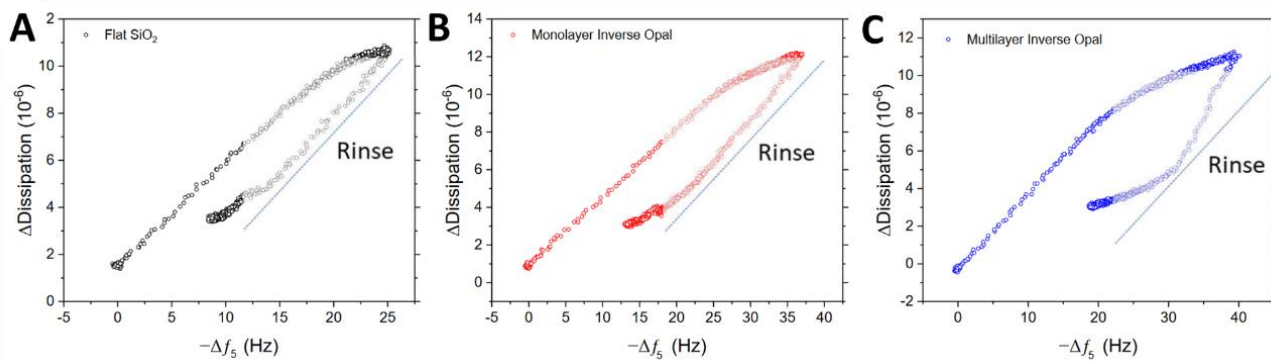


Figure 6: Comparing dissipation response as a function of frequency change across inverse opal functionalised surfaces. Response analysis using (A) flat silica, (B) silica inverse opal monolayer and (C) silica inverse opal multilayer substrates towards  $1 \times 10^9$  ESPs/mL in 25% v/v serum.

the impact on detection sensitivity. Data for both frequency and dissipation response are shown in **Figure 7**. Interestingly, multilayer IOs seemed to exhibit stronger responses across all tested ESP concentrations for both methods of measurement, as well as increasing the dynamic range of detection compared to flat silica. It is likely that the increased internal surface area of the IO supports additional antibody functionalisation and subsequent exosome capture. It is also apparent that frequency responses for all three surfaces converged at the highest concentration of ESPs, perhaps as the sensors near saturation (**Figure 7A**). Conversely, dissipation response for multilayer IOs continued to increase and at a faster rate than the flat silica or monolayer IO (**Figure 7B**).

**Table 1** compares the LOD of the silica-based sensors. IO structures were shown to improve detection performance towards ESPs, with high surface area multilayer IOs demonstrating a frequency and dissipation LOD as low as  $6.24 \times 10^7$  and  $6.91 \times 10^7$  ESPs/mL respectively. These results should be evaluated alongside the findings of potential artefact and solvent entrapment in the multilayer 3D IOs compared to the monolayer 2D IOs. Thus, the observed improvement in performance is likely to a limited degree. Nonetheless, the combination of highly tuneable, scalable, and low-cost

fabrication of the IO structures underlines their potential to comprise a reliable method for improving QCM-D analytical performance.

LOD vs Sensor surface type			
Mode	Flat Silica	IO Monolayer	IO Multilayer
Frequency	$9.60 \times 10^7$	$9.24 \times 10^7$	$6.24 \times 10^7$
Dissipation	$9.01 \times 10^7$	$8.42 \times 10^7$	$6.91 \times 10^7$

Table 1: QCM-D LOD values calculated for the different silica surfaces used during this work.

## Conclusions

This work investigated the potential of inorganic IO networks for improved QCM-D biosensing performance. Vertical withdrawal and evaporative deposition techniques were employed as two co-assembly methods to produce silica IOs with monolayer (2D) and multilayer (3D) thickness, respectively. SEM characterisation confirmed some degree of shrinkage from the original colloidal sphere size, resulting in the formation of

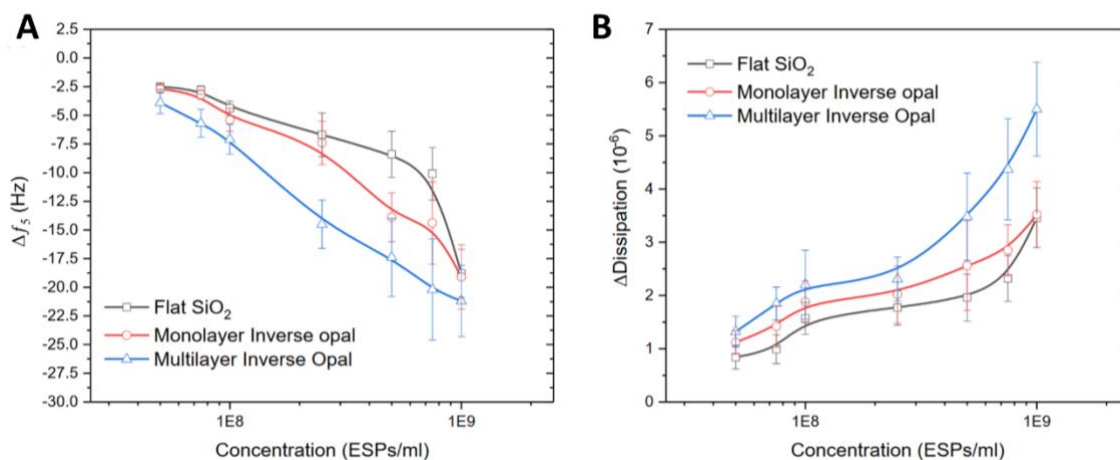


Figure 7: QCM-D performance comparison between flat silica, silica inverse opal monolayer and multilayer surfaces against titrated concentrations of ESPs spiked in 25% v/v serum. QCM-D (A) frequency and (B) corresponding dissipation profiles. Standard deviation is determined from three independent experiments.

oblate ellipsoidal pores. This allowed the internal surface area to be estimated as being 2-fold and 43-fold larger for monolayer and multilayer IOs respectively, compared to a flat silica surface. The generation of these structures on silica QCM sensors supported successful immunosensing of spiked CD63 protein, followed by CD63-positive exosomes. IO structures were shown to improve detection performance towards ESPs, with high surface area multilayer IOs demonstrating a frequency and dissipation LOD as low as  $6.24 \times 10^7$  and  $6.91 \times 10^7$  ESPs/mL respectively. However, possible findings of solvent and artefact entrapment within the 3D IO structures suggest that careful investigation of such systems is needed to validate their effectiveness. 2D IO surfaces on the other hand offer the scope for compartmentalised ligand and analyte anchoring. Furthermore, the fabrication and sensing strategies presented create opportunities for advanced dual-mode analysis of clinically relevant biomarkers by combining QCM-D with optical methods that exploit the photonic band gap properties of the IO architectures.

## Experimental

**Materials:** Materials for inverse opal formation include TEOS (98%, Sigma-Aldrich, USA), 250 nm and 600 nm poly(methyl methacrylate) (PMMA) (Microparticles GmbH, Germany). Si (100) wafers (p-type) were purchased from MicroChemicals GmbH and cut to appropriate dimensions (1x2 cm). An anti-mouse detection module for a WES machine and 12-230 kDa WES separation modules were acquired from Protein Simple (Biotechne, USA). For isolation and sample preparation, qEV original SEC columns (Izon Science, UK), 0.45  $\mu\text{m}$  filters (Merck Millipore, USA), HEPES buffered saline (HBS, 0.01M HEPES, pH 7.4, 0.15M NaCl) (GE Healthcare Life Sciences, Sweden), Amicon Ultra-15 centrifugal filters (Merck Millipore, USA), 100 nm polystyrene beads (Thermofisher Scientific, UK) and RIPA buffer (Sigma Aldrich, USA) were employed. Antibodies used in immunosensing and western blotting included mouse monoclonal anti-Alix (634502, Biologend UK), mouse monoclonal anti-CD63 (353013, Biologend UK), mouse monoclonal anti-CD81 (349501, Biologend UK), mouse monoclonal biotinylated-anti CD63 (353017, Biologend UK), biotin-IgG isotype control antibody (400103, Biologend UK). Streptavidin was acquired from Sigma Aldrich (USA). Silane-PEG (2 kDa)-biotin (Laysan Bio, USA) and silane-OEG (600 Da)-COOH (Nanocs, USA) were purchased for SAM formation on silica. Silica coated QCM sensors were purchased from QuartzPro, Sweden.

**Exosome isolation and characterisation:** SEC isolation of 10 x 1 mL ESPs fractions from human mesenchymal stem-cell cell-culture media (HUMSCCM) was conducted as detailed in previous studies.<sup>15</sup> Briefly, the source HUMSCCM was first filtered with a 0.45  $\mu\text{m}$  filter (Merck Millipore, U.S.). Thirty mL of clarified media was subsequently concentrated using Amicon Ultra-15 centrifugal filters with a 10 kDa pore size cutoff (Merck Millipore, USA). The filters were spun at 4000g for 30 min at 4 °C. Post spin, 0.5 mL of concentrated filtrate was loaded onto a qEV 35 nm SEC column (Izon Science, UK). 0.2  $\mu\text{m}$  filtered HEPES

buffered saline (HBS, 0.01 M HEPES, pH 7.4, 0.15 M NaCl) (GE Healthcare Life Sciences, Sweden) was used as the eluting buffer at a flow rate of 1 mL min<sup>-1</sup>. Ten 1 mL fractions were collected and stored at -80 °C. NTA analysis (Nanosight LM10 instrument, Malvern Instruments, UK) of SEC fractions was conducted as described in a previous study.<sup>12</sup> Exosome presence in HUMSCCM derived ESPs was verified through western blot analysis via capillary gel electrophoresis format as described in a previous study, using a WES instrument from Protein Simple (Biotechne Ltd., USA).<sup>12</sup> SEC fractions 3, 4, 5 and 6 were selected for analysis. Exosomal proteins Alix (97 kDa), tetraspannin CD63 (57 kDa) and CD81 (26 kDa) were probed by chemiluminescent immunoassay, using mouse monoclonal anti-Alix, mouse monoclonal anti-CD63 and mouse monoclonal anti-CD81 as primary antibodies.

**Colloidal suspension preparation:** A TEOS mixture consisting of 1:1:1.5 ratio (by weight) of TEOS, 0.10 M HCl, and EtOH (100%) was made. 0.15 mL of this mixture was added to 19.5 mL of deionised water and 0.5 mL of a 5% w/v colloidal PMMA particle (250 and 600 nm diameter) suspension in water (pre-dispersed by sonication). The solution was stirred for 1 h at room temperature prior to use.

**Monolayer formation via vertical withdrawal co-assembly:** Bare Si wafers (1 x 2 cm) and silica coated QCM sensors were exposed to 60 s of oxygen plasma (20 sccm) using a Diener Electronic PICO instrument, to remove organic contaminants and for oxide activation to introduce desirable hydrophilic properties for co-assembly. Si wafers and silica coated QCM sensors were suspended in a container of colloid/TEOS suspension using a custom-made motorised sample holder. The submerged sample was withdrawn at a programmed rate of 0.01 mm/min over 24 hours, inducing thin film deposition at the air-solvent interface. Post-deposition, wafers/sensors were annealed at 180 °C for 2 h to aid mechanical stability prior to removal of PMMA. The PMMA opal template was removed by oxygen reactive ion etching using oxygen plasma exposure for 300 s (20 sccm)

**Multilayer formation via vertical evaporative deposition co-assembly:** As before, bare Si wafers (1 x 2 cm) and silica coated QCM sensors were exposed to 60 s of oxygen plasma (20 sccm) using a Diener Electronic PICO instrument. Si wafer and silica coated QCM sensors were then suspended in a container of colloid/TEOS suspension using a custom-made sample holder. The colloidal suspension was evaporated over a 2-day period in a 65 °C oven, inducing film deposition at the air-solvent interface. Post-deposition, wafers/sensors were annealed at 180 °C for 2 h to aid mechanical stability prior to removal of PMMA. The opal substrates were then calcined in air at 500 °C for 2 h with a 4 h ramp time for the removal of PMMA and sintering of the silica inverse opal structures

**Scanning electron microscopy:** Si wafers with inverse opal films were analysed with SEM using a JEOL 6701 instrument (Japan). All micrographs were collected at an accelerating voltage of 10 kV. Samples were mounted for both cross-sectional and

longitudinal imaging on black carbon tape followed by gold sputter coating for 10 s at 0.08 mBarr prior to analysis. In-plane and out-of-plane pore size distributions were determined using the Pebbles software.<sup>56</sup>

**Grazing incidence small angle scattering:** GISAXS experiments were performed using a SAXSLab Ganesha 300XL (8 keV), as part of the Centre for Nature Inspired Engineering (CNIE) research facility service, University College London. The incident angle was set at 0.18°. 2D scattering patterns were collected with a PILATUS 300K solid-state photon-counting detector at a sample-to-detector distance of 1400 mm. GISAXS data analysis was performed using FitGISAXS software.<sup>57</sup> Si wafers with inverse opals formed from 100 nm PMMA spheres using the evaporative deposition approach were used for analysis to understand the structural order of the pores.

**General QCM apparatus setup:** All QCM-D measurements in this work were carried out using a Q-Sense E4 instrument (Biolin Scientific, Sweden). Analysis of frequency and dissipation response was conducted using the QTools software, version 3.0.17.560 (Biolin Scientific, Sweden). Changes in resonance frequency ( $\Delta f$ ) were recorded from the third, fifth, seventh, ninth and eleventh overtones. The presented data relate to the 5th overtone, with variation of  $\Delta f$  between overtones being 10% or less. In all instances, samples were degassed prior to exchange in the QCM flow module and AT-cut 5-MHz gold coated quartz crystal sensors with a 0.79 cm<sup>2</sup> active area (Biolin, Sweden) were used. The reproducibility of the fabrication process was ensured by preparing all analytes using the same HEPES buffered saline (HBS) stock solution or serum stock to minimise impact of buffer properties during sample exchange. These were prepared to identical volumes (0.25 mL per sensor). All reagents were sourced from the same suppliers throughout the study to avoid influences of differing characteristics or quality. In all cases, the analyte was flowed at 10  $\mu$ L/min and a sensor was routinely reserved for baseline measurement, to account for drift and background changes induced by buffer exchange. Frequency and dissipation responses are reported net or post-buffer rinse, to account for the removal of weakly bound analytes.

**Silica-coated QCM sensor functionalisation:** A 5 mM solution of silane-PEG (2 kDa)-Biotin and spacer molecule silane-PEG (600 Da)-COOH at a 1:9 molar ratio was flowed across the sensor surface at 7.5  $\mu$ L/min overnight to form a mixed SAM. A 100  $\mu$ g/mL solution of SAV was flowed across the sensor surface at 10  $\mu$ L/min for 20 minutes, followed by a rinse step of HBS at 80  $\mu$ L/min for 15 minutes. 20  $\mu$ g/mL of mouse monoclonal biotinylated-anti CD63 was immobilised on the surface at 10  $\mu$ L/min for 20 minutes, followed by another rinse step and response stabilisation for 30 minutes prior to sample addition.

**QCM-D immunodetection of exosomes using silica sensors:** Silica based immunosensor functionality towards spiked CD63 and exosomal CD63 was assessed. Spiked samples of CD63 tetraspannin protein with a concentration of 35 nM were used as a positive control. Sensitivity towards CD63-positive

exosomes in HBS buffer was tested using dilutions of SEC fraction 4. ESP samples were titrated in 25% v/v human serum (Sigma Aldrich, USA) to determine the sensitivity of the platform in complex media. The sensors were assessed with the following concentrations: 5x10<sup>7</sup>, 7.5x10<sup>7</sup>, 1x10<sup>8</sup>, 2.5x10<sup>8</sup>, 5x10<sup>8</sup>, 7.5x10<sup>8</sup> and 1x10<sup>9</sup> ESPs/mL. Specificity of the sensor surfaces, and background signal were determined by replacing the anti-CD63 antibody with a biotin-IgG isotype control antibody. Response was compared between sensor surfaces using a concentration of 1x10<sup>9</sup> ESPs/mL in HBS buffer and 25% v/v serum. LOD and LOQ were defined as the minimum concentration displaying a signal-to-noise ratio of 3 and 10 respectively.<sup>58</sup> SNR was determined as a ratio of the response elicited on the target and control sensor surfaces.

## Author Contributions

JS and AAF conceptualized the IO fabrication and sensing application. JS, AT and AAF participated in the fabrication of the IO architectures. JS performed QCM-D and SEM experiments. AAF performed SEM image analysis and SAXS experiments. The initial draft was written by AAF and JS and edited by SG, AT and GW. The project was supervised throughout by SG and GW.

## Conflicts of interest

There are no conflicts to declare.

## Acknowledgements

The authors thank the Engineering and Physical Sciences Research Council (EPSRC) for provision of a studentship to J.S. on the Centre for Doctoral Training in Advanced Therapeutics and Nanomedicines (EP/L01646X), as well as for funding on an EPSRC New Investigator Award (EP/R035105/1). We further acknowledge the Medical Research Council (MRC, MR/R000328/1), for financial support. The authors also thank Dr. Benjamin Weil and Prof. Mark Lowdell from the Centre for Cell, Gene, and Tissue Therapeutics at the Royal Free London NHS Foundation Trust, for donating the HUMSCCM used in this research.

## Notes and references

- 1 E. Cocucci and J. Meldolesi, *Trends in Cell Biology*, 2015, **25**, 364–372.
- 2 G. van Niel, G. D'Angelo and G. Raposo, *Nature Reviews Molecular Cell Biology*, 2018, **19**, 213–228.
- 3 S. Keerthikumar, D. Chisanga, D. Ariyaratne, H. al Saffar, S. Anand, K. Zhao, M. Samuel, M. Pathan, M. Jois, N. Chilamkurti, L. Gangoda and S. Mathivanan, *Journal of Molecular Biology*, 2016, **428**, 688–692.
- 4 C. Rajagopal and K. B. Harikumar, *Frontiers in Oncology*, 2018, **8**, 66.
- 5 J. Skog, T. Würdinger, S. van Rijn, D. H. Meijer, L. Gainche, W. T. Curry, B. S. Carter, A. M. Krichevsky and X. O. Breakefield, *Nature Cell Biology*, 2008, **10**, 1470–1476.

- 6 G. Mao, Z. Zhang, S. Hu, Z. Zhang, Z. Chang, Z. Huang, W. Liao and Y. Kang, *Stem Cell Research and Therapy*, 2018, **9**, 247.
- 7 C. Z. J. Lim, Y. Zhang, Y. Chen, H. Zhao, M. C. Stephenson, N. R. Y. Ho, Y. Chen, J. Chung, A. Reilhac, T. P. Loh, C. L. H. Chen and H. Shao, *Nature Communications*, 2019, **10**, 1144.
- 8 A. Accardo, L. Tirinato, D. Altamura, T. Sibillano, C. Giannini, C. Riekel and E. di Fabrizio, *Nanoscale*, 2013, **5**, 2295–2299.
- 9 X. Zhao, W. Zhang, X. Qiu, Q. Mei, Y. Luo and W. Fu, *Analytical and Bioanalytical Chemistry*, 2020, **412**, 601–609.
- 10 Z. Weng, S. Zong, Y. Wang, N. Li, L. Li, J. Lu, Z. Wang, B. Chen and Y. Cui, *Nanoscale*, 2018, **10**, 9053–9062.
- 11 S. Jeong, J. Park, D. Pathania, C. M. Castro, R. Weissleder and H. Lee, *ACS Nano*, 2016, **10**, 1802–1809.
- 12 J. Suthar, E. S. Parsons, B. W. Hoogenboom, G. R. Williams and S. Guldin, *Analytical Chemistry*, 2020, **92**, 4082–4093.
- 13 I. Reviakine, D. Johannsmann and R. P. Richter, *Analytical Chemistry*, 2011, **83**, 8838–8848.
- 14 C. Wang, C. Wang, D. Jin, Y. Yu, F. Yang, Y. Zhang, Q. Yao and G. J. Zhang, *ACS Sensors*, 2020, **5**, 362–369.
- 15 J. Suthar, B. Prieto-Simon, G. R. Williams and S. Guldin, *Analytical Chemistry*, 2022, **94**, 2465–2475.
- 16 S. J. Yeo, G. H. Choi and P. J. Yoo, *Journal of Materials Chemistry A*, 2017, **5**, 17111–17134.
- 17 A. Stein, F. Li and N. R. Denny, *Chemistry of Materials*, 2008, **20**, 649–666.
- 18 A. Stein, B. E. Wilson and S. G. Rudisill, *Chemical Society Reviews*, 2013, **42**, 2763–2803.
- 19 B. Hatton, L. Mishchenko, S. Davis, K. H. Sandhage and J. Aizenberg, *Proc Natl Acad Sci U S A*, 2010, **107**, 10354–10359.
- 20 G. Collins, M. Blömker, M. Osiak, J. D. Holmes, M. Bredol and C. O'Dwyer, *Chemistry of Materials*, 2013, **25**, 4312–4320.
- 21 G. A. Umeda, W. C. Chueh, L. Noailles, S. M. Haile and B. S. Dunn, *Energy & Environmental Science*, 2008, **1**, 484–486.
- 22 G. I. N. Waterhouse and M. R. Waterland, *Polyhedron*, 2007, **26**, 356–368.
- 23 S. Yeon Lee, S.-H. Kim, H. Hwang, J. Young Sim, S.-M. S. Yang Y Lee, S. Kim, H. Hwang, J. Y. Sim, S. Yang and S. Y. Lee, *Advanced Materials*, 2014, **26**, 2391–2397.
- 24 C. Y. Cho and J. H. Moon, *Langmuir*, 2012, **28**, 9372–9377.
- 25 X. Chen, Y. Wang, J. Zhou, W. Yan, X. Li and J. J. Zhu, *Analytical Chemistry*, 2008, **80**, 2133–2140.
- 26 S. Guldin, S. Hüttner, M. Kolle, M. E. Welland, P. Müller-Buschbaum, R. H. Friend, U. Steiner and N. Tétreault, *Nano Letters*, 2010, **10**, 2303–2309.
- 27 H. Wang, Y. F. Lu and Z. Y. Yang, <https://doi.org/10.1117/12.644976>, 2006, **6107**, 129–135.
- 28 N. Bowden, S. Brittain, A. G. Evan, J. W. Hutchinson, G. M. White, B. H. Beatriz Juprez, D. Golmayo, P. A. Postigo, C. López, C. López, B. H. Juprez, D. Golmayo and P. A. Postigo, *Advanced Materials*, 2004, **16**, 1732–1736.
- 29 G. I. N. Waterhouse and M. R. Waterland, *Polyhedron*, 2007, **26**, 356–368.
- 30 M. Schaffner, G. England, M. Kolle, J. Aizenberg and N. Vogel, *Small*, 2015, **11**, 4334–4340.
- 31 L. Mishchenko, B. Hatton, M. Kolle, J. Aizenberg, L. Mishchenko, B. Hatton, M. Kolle and J. Aizenberg, *Small*, 2012, **8**, 1904–1911.
- 32 B. Hatton, L. Mishchenko, S. Davis, K. H. Sandhage and J. Aizenberg, *Proc Natl Acad Sci U S A*, 2010, **107**, 10354–9.
- 33 A. Alvarez-Fernandez, M. J. Fornerod, B. Reid and S. Guldin, *Langmuir*, 2022, **38**, 3297–3304.
- 34 B. Reid, A. Alvarez-Fernandez, B. Schmidt-Hansberg and S. Guldin, *Langmuir*, 2019, **35**, 14074–14082.
- 35 H. N. Lokupitiya, A. Jones, B. Reid, S. Guldin and M. Stefik, *Chemistry of Materials*, 2016, **28**, 1653–1667.
- 36 A. Sarkar, A. Thyagarajan, A. Cole and M. Stefik, *Soft Matter*, 2019, **15**, 5193–5203.
- 37 A. Alvarez-Fernandez, B. Reid, J. Suthar, S. Y. Choy, M. Jara Fornerod, N. mac Fhionnlaoich, L. Yang, B. Schmidt-Hansberg and S. Guldin, *Nanoscale*, 2020, **12**, 18455–18462.
- 38 F. Fathi, M. R. Rashidi, P. S. Pakchin, S. Ahmadi-Kandjani and A. Nikniazi, *Talanta*, 2021, **221**, 121615.
- 39 J. Li, X. Zhao, H. Wei, Z. Z. Gu and Z. Lu, *Analytica Chimica Acta*, 2008, **625**, 63–69.
- 40 W. Lee, T. Kang, S.-H. Kim and J. Jeong, *Sensors*, 2018, **18**, 307.
- 41 Y. Jiang, C. Cui, Y. Huang, X. Zhang and J. Gao, *Chemical Communications*, 2014, **50**, 5490–5493.
- 42 A. Chiappini, L. Pasquardini, S. Nodehi, C. Armellini, N. Bazzanella, L. Lunelli, S. Pelli, M. Ferrari and S. Pietralunga, *Sensors*, 2018, **18**, 4326.
- 43 S. Dong, Y. Wang, Z. Liu, W. Zhang, K. Yi, X. Zhang, X. Zhang, C. Jiang, S. Yang, F. Wang and X. Xiao, *ACS Applied Materials and Interfaces*, 2020, **12**, 5136–5146.
- 44 D. Y. Choi, J. C. Yang and J. Park, *Sensors and Actuators B: Chemical*, 2022, **350**, 130855.
- 45 D. K. Oh, J. C. Yang, S. W. Hong and J. Park, *Sensors and Actuators B: Chemical*, 2020, **323**, 128670.
- 46 L. Pol, C. Eckstein, L. K. Acosta, E. Xifré-Pérez, J. Ferré-Borrull and L. F. Marsal, *Nanomaterials 2019, Vol. 9, Page 478*, 2019, **9**, 478.
- 47 N. Asai, N. Matsumoto, I. Yamashita, T. Shimizu, S. Shingubara and T. Ito, *Sens Biosensing Res*, 2021, **32**, 100415.
- 48 N. Asai, T. Shimizu, S. Shingubara and T. Ito, *Sensors and Actuators B: Chemical*, 2018, **276**, 534–539.
- 49 P. I. Reyes, Z. Duan, Y. Lu, D. Khavulya and N. Boustany, *Biosensors and Bioelectronics*, 2013, **41**, 84–89.
- 50 P. N. Bartlett, J. J. Baumberg, P. R. Birkin, M. A. Ghanem and M. C. Netti, *Chemistry of Materials*, 2002, **14**, 2199–2208.
- 51 Y. G. Seo, K. Woo, J. Kim, H. Lee and W. Lee, *Advanced Functional Materials*, 2011, **21**, 3094–3103.
- 52 H. Míguez, N. Tétreault, B. Hatton, S. M. Yang, D. Perovic and G. A. Ozin, *Chemical Communications*, 2002, **2**, 2736–2737.
- 53 S. Mondini, A. M. Ferretti, A. Puglisi and A. Ponti, *Nanoscale*, 2012, **4**, 5356.
- 54 B. T. Holland, C. F. Blanford, A. Stein and M. Greenblatt, *Chemtracts*, 1999, **12**, 121–124.
- 55 Y. Xia, B. Gates, Y. Yin and Y. Lu, *Advanced Materials*, 2000, **12**, 693–713.
- 56 S. Mondini, A. M. Ferretti, A. Puglisi and A. Ponti, *Nanoscale*, 2012, **4**, 5356–5372.
- 57 D. Babonneau, *Journal of Applied Crystallography*, 2010, **43**, 929–936.
- 58 A. Shrivastava and V. Gupta, *Chronicles of Young Scientists*, 2011, **2**, 21.